

Adaptive Channel-State-Information Feedback in Integrated Sensing and Communication Systems

Neeraj Varshney, Samuel Berweger, Jack Chuang, Steve Blandino, Jian Wang, Neha Pazare, Camillo Gentile, and Nada Golmie

Abstract—Efficient design of integrated sensing and communication systems can minimize signaling overhead by reducing the size and/or rate of feedback in reporting channel state information (CSI). To minimize the signaling overhead when performing sensing operations at the transmitter, this paper proposes a procedure to reduce the feedback rate. We consider a threshold-based sensing measurement and reporting procedure, such that the CSI is transmitted only if the channel variation exceeds a threshold. However, quantifying the channel variation, determining the threshold, and recovering sensing information with a lower feedback rate are still open problems. In this paper, we first quantify the channel variation by considering several metrics including the Euclidean distance, time-reversal resonating strength, and frequency-reversal resonating strength. We then design an algorithm to adaptively select a threshold, minimizing the feedback rate, while guaranteeing sufficient sensing accuracy by reconstructing high-quality signatures of human movement. To improve sensing accuracy with irregular channel measurements, we further propose two reconstruction schemes, which can be easily employed at the transmitter in case there is no feedback available from the receiver. Finally, the sensing performance of our scheme is extensively evaluated through real and synthetic channel measurements, considering channel estimation and synchronization errors. Our results show that the amount of feedback can be reduced by 50% while maintaining good sensing performance in terms of range and velocity estimations. Moreover, in contrast to other schemes, we show that the Euclidean distance metric is better able to capture various human movements with high channel variation values.

Index Terms—802.11bf, 802.11ay pilots, communication waveform, human motion, sensing, target detection, threshold

I. INTRODUCTION

THE PARADIGM of integrated sensing and communication (ISAC), in which sensing and communication systems are integrated to efficiently utilize congested radio resources [1], [2], has received significant research interest

in recent years. The ISAC paradigm is envisioned to utilize common hardware and spectrum resources, as well as a common signal, to perform both communication and sensing tasks. This in turn improves spectral and energy efficiencies without increasing the hardware and signaling costs towards realizing the future pervasive intelligent networks in the sixth generation (6G) systems. In particular, ISAC systems improve efficiency by either realizing sensing-assisted communication or communication-assisted sensing [3]. In the latter case, the existing wireless networking infrastructure for the Internet of Things (IoT) systems can be reused as a sensor network to enable ground-breaking wireless sensing applications for healthcare, enterprise, residential, retail, and hospitality industries [4] through the communication waveforms. In general, communication-assisted sensing or sensing-assisted communication in ISAC systems can be realized by tracking the variation in the channel due to a changing physical environment that alters the signal propagation paths. In ISAC systems, this tracking is possible by utilizing the channel estimated using the pilot sequences embedded in the data packets [5].

Recently, the IEEE has started an effort toward 802.11bf Wi-Fi sensing, a new specification [6] that will turn most of the existing 802.11 wireless local area network (WLAN) devices into object sensors to measure the range, speed, and direction of objects and people while maintaining the communication functionality. In contrast to the broader wireless sensing research effort, which focuses on building prototypes and designing algorithms to provide better sensing solutions, the development of the IEEE 802.11bf standards defines sensing procedures and protocols to discover available devices for sensing, forming sensing groups, defining required sensing measurements, and feeding back sensing results [6], [7].

To realize these functionalities, several roles such as sensing initiator, responder, transmitter, and receiver are defined in [6].

- **Initiator:** An initiator is a device that initiates the sensing procedure and wants the sensing result.
- **Responder:** A responder is a non-initiator device that participates in the sensing procedure to assist the initiator.
- **Transmitter:** A responder, which acts as a transmitter, transmits packets for measurement.
- **Receiver:** A responder, which acts as a receiver, utilizes the packets transmitted by a transmitter to obtain the sensing measurements (e.g., raw channel state information (CSI) or channel impulse response (CIR), received waveform).

N. Varshney (neeraj.varshney@nist.gov) is research associate with the Radio Access and Propagation Metrology Group, National Institute of Standards and Technology (NIST), Gaithersburg, MD 20899-6730 USA and contractor with Prometheus Computing LLC, Cullowhee, NC USA.

J. Chuang, J. Wang, and C. Gentile are with the Radio Access and Propagation Metrology Group, National Institute of Standards and Technology, Gaithersburg, MD 20899-6730 USA (E-mail: {name.surname}@nist.gov).

S. Blandino (steve.blandino@nist.gov) is research associate with the Radio Access and Propagation Metrology Group, National Institute of Standards and Technology (NIST), Gaithersburg, MD 20899-6730 USA and contractor with Prometheus Computing LLC, Cullowhee, NC USA.

N. Pazare (neha.pazare@nist.gov) is with the Department of Electrical Engineering, University of Colorado, Boulder, Colorado 80309, USA.

S. Berweger and N. Golmie are with the Communications Technology Laboratory, National Institute of Standards and Technology, Gaithersburg, MD 20899-6730 USA (E-mail: {name.surname}@nist.gov).

Copyright © 2023 IEEE. Personal use of this material is permitted. However, permission to use this material for any other purposes must be obtained from the IEEE by sending a request to pubs-permissions@ieee.org.

A. Motivation and Related Work

An underlying condition for ISAC networks is that at least one of the devices can perform sensing processing. If the receiver has sensing processing capabilities, it can directly process the sensing measurements and feed back the final sensing result to the initiator after Doppler signal processing (e.g., range-Doppler map, range-time map). In contrast, if only the transmitter has the sensing processing capabilities, the receiver can send back over the air the requested measurements, which enables the transmitter to obtain the final sensing result after processing. In the latter case, the sensing accuracy at the transmitting device strongly depends on the availability and update rate of the sensing measurements, such as CSI or CIR. As the IEEE 802.11bf re-uses the communication link, sending and exchanging sensing information can be solely seen as overhead from a Wi-Fi performance point-of-view, reducing throughput and increasing latency. In this case, the larger the overhead, the better the sensing accuracy will be at the cost of a lower transmission data rate. Thus, an efficient design of communication-assisted sensing in an ISAC network must minimize the communication overhead associated with transmitting sensing measurements while obtaining reasonable sensing performance.

There are several sensing sources [5], e.g., received signal strength (RSS), CSI, and the received waveform, *i.e.*, the measurement used to obtain sensing information, but in this work we consider CSI. Assuming the CSI is used to perform sensing, there are two main strategies that can minimize the impact of the feedback. The first strategy consists in reducing the size of the feedback. For instance, it is possible to report a partial CSI, corresponding to the range of interest of the entire CSI [8]. This scheme is known as truncated CIR-based measurement and reporting, where only the subset of complex samples corresponding to the range of interest of the entire CIR is reported to the initiator or processor. A second strategy consists of reducing the rate of the feedback. For example, in non-time sensitive applications such as intruder detection, several measurements might be highly correlated over a period of time and do not require frequent and regular CSI feedback. To address this issue, 802.11bf task group (TGBf) [6] recently introduced a threshold-based sensing measurement and reporting (TSMR) procedure for sub-6 GHz bands where the current CIR measurement can only be feedback by the receiver if CSI variation is above a given threshold [9]. However, a clear definition of CSI variation, *i.e.*, a metric quantifying the difference between the current measured CSI and previously measured CSI as well as the selection of threshold without understanding the definition of CSI variation are missing [10]. Moreover, a clear explanation of what should be done to capture the micro-Doppler signature if we have irregular channel measurements at the transmitter is also missing. Further, to the best of our knowledge, the impact of this TSMR procedure on sensing performance has not been investigated yet in the existing literature. To fill these gaps as well as address the aforementioned issues, this paper comprehensively analyzes the performance of threshold-based sensing using the communication waveform. Particularly, we

utilize the channel estimated through pilot sequences [11] while having a communication link between two nodes.

To summarize, the key contributions of this paper are as follows.

- First, we describe the TSMR procedure, where we consider one-bit feedback from the receiver to the transmitter to indicate that CSI variation is above or below the threshold. We consider three different metrics, namely the Euclidean distance, time-reversal (TR) resonating strength, and frequency-reversal (FR) resonating strength, to analyze their impact on CSI variation under several human movement conditions. If CSI variation is not significant (*i.e.*, CSI variation is below a threshold), the transmitter reconstructs the missing CIR measurement at the initiator. In this context, we propose two different reconstruction schemes, *i.e.*, previous measurement-based reconstruction and linear interpolation-based reconstruction to develop high-quality or realistic micro-Doppler signatures of human movements.
- Second, we propose an adaptive threshold scheme, which can be considered at the initiator to update the threshold adaptively by detecting the variations in the channel through previously received CIR measurements. This scheme results in improved sensing performance in comparison to the fixed threshold while reducing the number of feedback messages.
- Third, we study various types of model- and measurement-based human motion to leverage realistic insight in development of the said algorithms. More specifically, to analyze performance, we start with a raytracing-based channel model and validate the results with real channel measurements obtained through an extensive channel measurement campaign, which we recently conducted to enable analyzing the sensing performance considering different human movements of several human subjects in a more realistic scenario.

B. Organization

The organization of this paper is as follows. Section II describes the Wi-Fi sensing system model including definition of the transmitter and receiver signals, the channel model, and all the ISAC processing required to analyze the system performance. The complete TSMR procedure and adaptive threshold-based scheme are described in detail in Section III and Section IV, respectively, which utilizes the communication waveform to transmit a packet including data and preamble with pilot sequences. Based on the NIST raytracing-based channel model for an indoor living room scenario with a single human target and the NIST human tracking channel measurement, performance evaluation results are presented in Section V, followed by the conclusions in Section VI.

II. WI-FI SENSING SYSTEM MODEL AND SIGNAL PROCESSING

This section begins with describing the Wi-Fi sensing system model adopted for ISAC framework, including all

the ISAC signal processing required to analyze the end-to-end sensing performance in terms of range and velocity or Doppler shift of the human target under channel estimation and synchronization errors.

A. System Model with Imperfect Channel Estimates

Sensing can be achieved using the illumination offered by communication signals, *i.e.*, communication devices can act as sensing nodes, using the principles of bi-static or multistatic radar [12]. Hence, we consider an ISAC system, adopting a conventional communication system model, consisting of a single transmitting device and a single receiving device. From a sensing perspective this system is referred to as a bi-static model, as the transmitter and the receiver do not correspond to the same device and they can be spatially separated, as in the ISAC system presented in Fig. 1.

1) *Transmit Signal*: We consider a wideband single-carrier (SC) system, where the transmitter transmits a total of N_{burst} bursts continuously without any pause between adjacent bursts. Each burst consists of M packets, which are transmitted to the receiver over a period of time T with packet repetition interval (PRI) T_M . This implies that the time interval between the start of adjacent bursts is just T , which equals MT_M . The channel during the time T is assumed to be quasi-static. The time T is usually referred to as coherent processing interval (CPI), as it enables the coherent processing of multiple receive packets. Each of the packet is made of two main parts: the preamble and the data. The preamble contains known pilot sequences, *e.g.*, Golay sequences, while the data contains modulated information symbols. As in this paper we are focusing on a sensing feature, for ease of exposition we provide the transmit model of the preamble, containing pilot sequences. Denoting $s[n]$ as the n^{th} symbol of the pilot with condition $|s[n]|=1$, the complex-baseband transmit symbols of the m^{th} packet can be written as

$$x_m[k] = \sum_{n=0}^{N-1} s[n] \delta(kT_S - nT_S - mT_M), \quad (1)$$

where N is the length of the preamble sequence, k is the sampling index, T_S is the sampling interval in the delay domain, also referred as *fast-time*, and T_M is the PRI in time domain, also referred as *slow-time*.

2) *Channel*: The channel of a static environment with moving targets is modeled as a superposition of rays, some describing the propagation of the signal in the environment, the other describing the backscattering signal generated from the target as shown in Fig. 1. The CIR considering the human presence in the environment with fixed communicating nodes can be expressed as

$$h_m(\tau) = \sum_{p=1}^{N_r} a_{m,p} \exp(-j2\pi\nu_{m,p}mT_M) \delta(\tau - \tau_{m,p}), \quad (2)$$

where N_r is the total number of rays, $a_{m,p}$ represents the complex amplitude of the p^{th} ray and the parameters $\tau_{m,p}$ and $\nu_{m,p}$ are the delay and the Doppler shift of the p^{th} ray,

respectively. The CIR $h_m(\tau)$ in Eq. (2) describes the propagation channel, without including the effect of the system. It can be converted into the system level CIR by applying antenna effects, band-limiting filters and system rate re-sampling [13] as

$$h_m[k] = \sum_{l=0}^{L_m-1} a_{m,l} \exp(-j2\pi\nu_{m,l}mT_M) \delta(kT_S - \tau_{m,l}), \quad (3)$$

where L_m is the length of the system level CIR $\mathbf{h}_m = [h_m[0], h_m[1], \dots, h_m[L_m-1]]^T$, over which the m^{th} packet is transmitted.

3) *Receive Signal*: The transmit signal interacts with the environment, including the moving targets. The k^{th} receive complex symbol of the preamble of the m^{th} packet can be expressed as

$$y_m[k] = \sum_{l=0}^{L_m-1} h_m[l] x_m[k-l] + z_m[k], \quad (4)$$

where $z_m[k] \sim \mathcal{N}(0, \sigma^2)$ is the additive white Gaussian noise (AWGN) with variance σ^2 . We assume that the channel is static during the transmission of a packet.

B. ISAC Processing

1) *Synchronization (Sync)*: The preamble is first used for temporal synchronization between the transmitter and the receiver. Synchronization is achieved by cross-correlating the known transmitted pilot symbols with the received symbols. The magnitude of the cross-correlator output consists of a sequence of large peaks – one for each delay bin in which at least one ray falls –, and several small peaks due to AWGN and imperfect auto-correlation properties. The synchronization is then referenced to the delay bin in which the maximum cross-correlation value falls. The fast-time index of this value corresponds to the propagation delay of the direct line-of-sight (LOS) path between transmitter and receiver. While in a monostatic or quasi-monostatic configuration the synchronization point can be used as the absolute propagation delay reference, in a bi-static configuration the absolute value of the propagation delay need to be estimated. Method for time estimation have been proposed and standardized, for instance IEEE 801.11-2016 standard incorporates a new protocol for estimating the propagation time between devices, the so-called fine time measurement (FTM) protocol [11]. We hence assume that the propagation time between devices is known, for instance, using time-stamping provided by FTM message exchange.

2) *CSI Acquisition and Feedback*: The preamble is further used at the receiver for obtaining the CSI, *i.e.* the time-domain CIR, using a channel estimation procedure as described below.

The pilot sequence $\{s[n]\}$ used in Eq. (1) consists of two sets of 256-sample Golay complementary sequence pair, denoted as \mathbf{G}_u and \mathbf{G}_v respectively [11, Section 28.10], with $\mathbf{G}_u = [-b_{128} \ -a_{128} \ b_{128} \ -a_{128}]$ and $\mathbf{G}_v = [-b_{128} \ a_{128} \ -b_{128} \ -a_{128}]$. The length of the Golay sequence L_G is 128, and the length of the complementary Golay sequence (*e.g.*, $[-b_{128} \ -a_{128}]$), is denoted as $L_{GC} = 256$. To obtain the

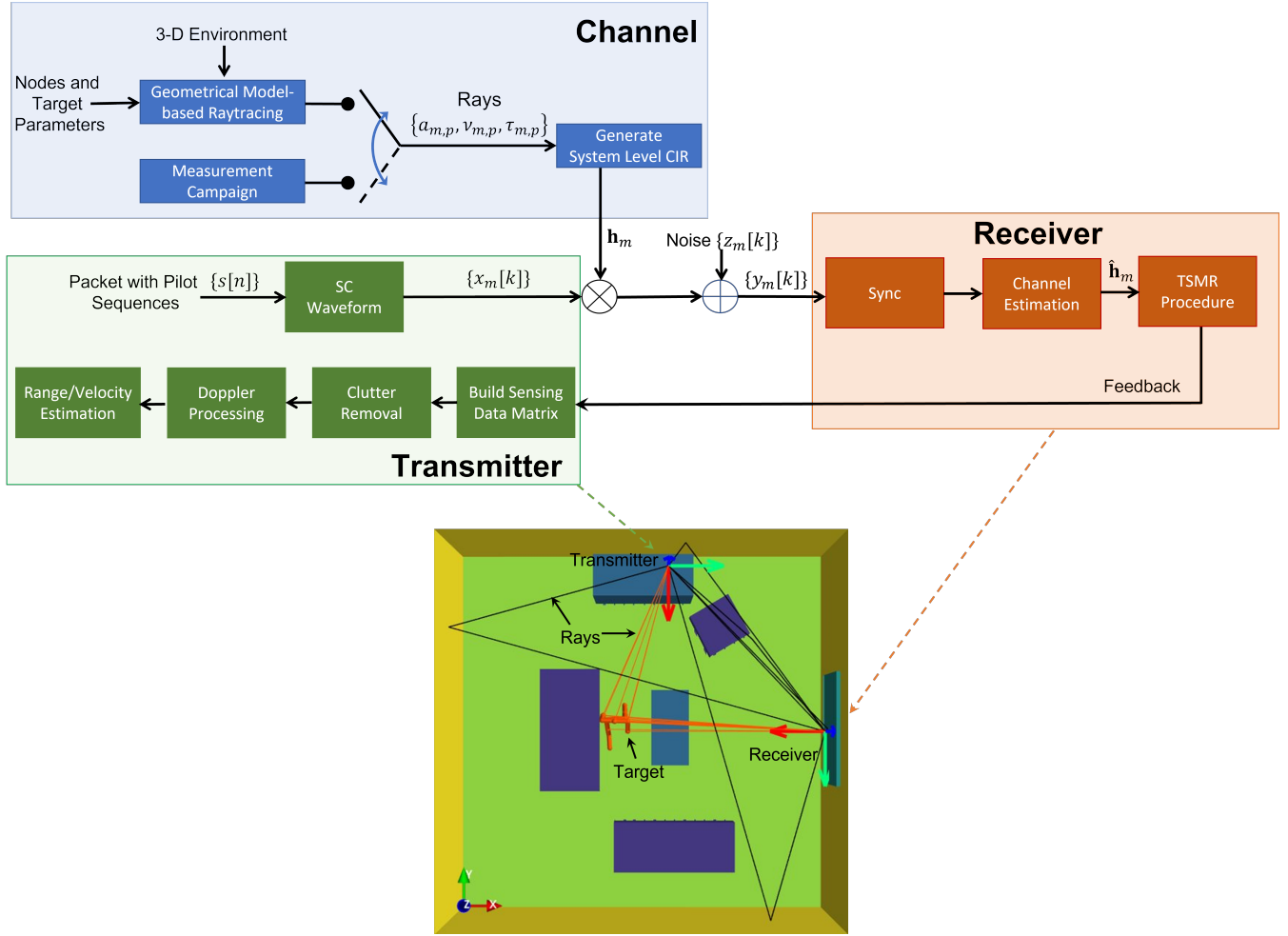


Fig. 1: Schematic diagram of a bistatic ISAC system model consisting of a single transmitter and receiver pair.

channel, the received symbols are correlated with \mathbf{G}_u and \mathbf{G}_v , and the correlations are summed as the following

$$\begin{aligned} \hat{h}_m[k] = & \sum_{j=0}^1 R_{\mathbf{G}_u, \mathbf{y}_m}[k + j \times L_{GC}] \\ & + \sum_{j=2}^3 R_{\mathbf{G}_v, \mathbf{y}_m}[k + j \times L_{GC}], \end{aligned} \quad (5)$$

where $R_{\mathbf{G}, \mathbf{y}_m}$, $\mathbf{G} \in \{\mathbf{G}_u, \mathbf{G}_v\}$ is the correlation between \mathbf{G} and \mathbf{y}_m and k^{th} entry of $R_{\mathbf{G}, \mathbf{y}_m}$ can be obtained as

$$R_{\mathbf{G}, \mathbf{y}_m}[k] = (\mathbf{G} * \tilde{\mathbf{y}}_m)[k], \quad (6)$$

where $\tilde{\mathbf{y}}_m$ is the time reversed and conjugated version of \mathbf{y}_m . After searching through \hat{h}_m and locating the peak index $l_m = \arg \max_k (|\hat{h}_m[k]|^2)$, the final estimated channel $\hat{\mathbf{h}}_m \in \mathbb{C}^{L_G \times 1}$ is extracted directly from index l_m with

$$\begin{aligned} \hat{\mathbf{h}}_m = & \frac{1}{2L_{GC}} [\hat{h}_m[l_m], \hat{h}_m[l_m + 1], \\ & \dots, \hat{h}_m[l_m + L_G - 1]]^T. \end{aligned} \quad (7)$$

In this paper, we consider that the transmitter corresponds to the sensing processor, which is using CSI to sense the environment. Hence, after CSI acquisition, the receiver feeds

back the estimated CSI in a sequential manner, exploiting the channel reciprocity. Further, note that the receiver does not store any previously estimated CSI measurements except the last transmitted one. Thus, at the current time, the receiver has only the current estimated CSI $\hat{\mathbf{h}}_m$ as well as previously transmitted CSI $\hat{\mathbf{h}}_{m-1}$ to quantify the variation in the channel.

3) *Doppler Processing*: From a sensing perspective, the channel estimated using the preamble can be seen as echoes from the targets and the environment. The CSI varies between the reception of each packet, i.e. with the slow-time, due to the phase changes induced by the Doppler shifts of the targets. After receiving the feedback, the transmit sensing processor can ideally build the sensing data matrix, collecting the estimated CIR corresponding to each packet sent, in a 2-dimensional (2-D) matrix $[\hat{\mathbf{h}}_1, \hat{\mathbf{h}}_2, \dots, \hat{\mathbf{h}}_M]$, i.e., the delay and the evolution over the time. To obtain the Doppler of the targets assuming the estimated CIRs corresponding to M feedback, a discrete Fourier transform (DFT) is applied to each delay bin along the slow-time dimension of the sensing data matrix to obtain the Doppler matrix,

$$\mathbf{D}[k, \nu] = \frac{1}{\sqrt{N_\nu}} \sum_{m=1}^M \hat{h}_m[k] \exp(-j2\pi m T_M \nu / N_\nu), \quad (8)$$

where ν is the Doppler bin index and N_ν is the DFT size. Apart from this, the component with null frequency shifts are

considered static clutter, *i.e.*, echoes coming from the static environment, thus they are not relevant to remote monitoring or sensing. They can be filtered out by removing the continuous component along the slow-time dimension of the sensing data matrix before obtaining range-Doppler map.

The obtained range-Doppler map is subject to de-noise processing. For this purpose, the range-Doppler map is first thresholded to eliminate the noise floor and low-pass filtered with a 2-D Gaussian window. The threshold has been empirically set to 10 dB below the strongest peak observed in the range-Doppler map. After that, a peak detection algorithm is performed by comparing each pixel of the range-Doppler map to its neighbors. If the tested pixel has a higher value than the surrounding pixels, the tested pixel is declared as the local maximum. The local maxima are thus retained in the de-noised range-Doppler map $\hat{D}[k, \nu]$.

4) *Target Detection*: The detection of the target properties, *i.e.*, velocity and range, is performed using the de-noised range-Doppler map, which is generated using the sensing data matrix corresponding to a burst of M packets. To obtain the velocity estimation, the range-Doppler map is summed over the range dimension, obtaining the micro-Doppler spectrum as $\mu D = \sum_k \hat{D}[k, \nu]$. The point with the highest intensity in the micro-Doppler spectrum $\hat{\nu} = \max_{\nu}(\mu D)$ is the estimated Doppler shift, from which the velocity can be obtained as $\hat{v} = \hat{\nu}c/f_c$, where c and f_c denote the speed of light and carrier frequency, respectively. Similarly, the estimation of the range relies on the sum of the range-Doppler map over the Doppler domain, *i.e.* $\mu R = \sum_{\nu} \hat{D}[k, \nu]$ and the estimated range is the highest value in the obtained range spectrum, $\hat{r} = \max_k(\mu R)$. Finally, after processing the range-Doppler maps corresponding to the transmissions of a total of N_{burst} bursts, the range \hat{r} and velocity \hat{v} over a period of time can be obtained by stacking \hat{r} and \hat{v} , respectively.

III. THRESHOLD-BASED SENSING MEASUREMENT AND REPORTING (TSMR) PROCEDURE

In this section, we first describe the possible sensing topologies or implementations involving two communicating devices and subsequently present the TSMR procedure including several CSI variation metrics and interpolation schemes for one of the implementations.

A. Sensing Topologies

Fig. 2 depicts two possible sensing implementations, which involve two devices or stations (STAs). In the first implementation, the initiator acts as a receiver and the responder acts as a transmitter. In this uplink case, the initiator can directly obtain the measurements using the packet transmitted by the responder. In the second implementation, the initiator acts as a transmitter and the responder acts as a receiver. In this downlink scenario, feedback from the receiver is required to report the CIR measurements to the initiator to perform sensing. The rate of feedback in the second implementation depends on the use case. Use cases, such as intruder detection, require sensing the environment continuously; however, they need to report feedback only when an event is detected.

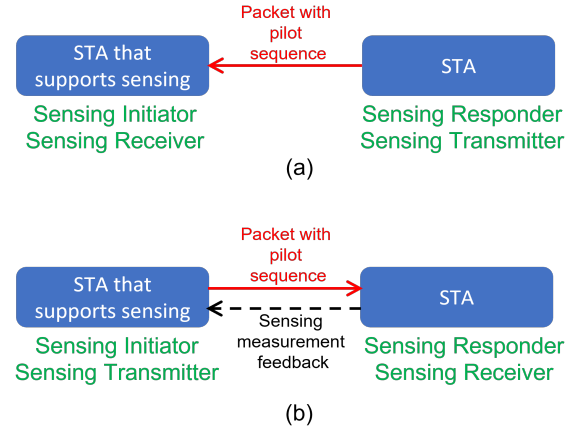


Fig. 2: Sensing implementations involving two STAs where the STA that supports sensing has the processing capability.

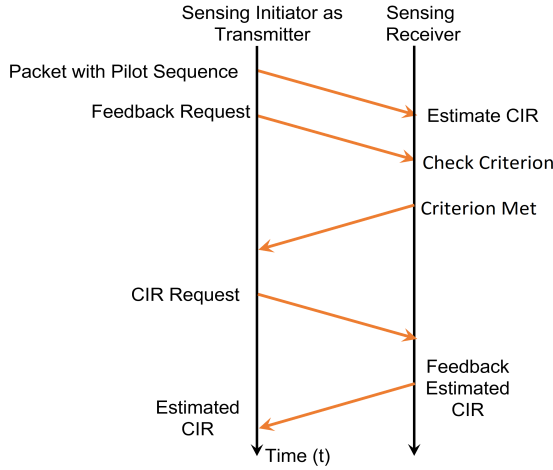
Otherwise, when no events are detected, the CSI is highly correlated over time and thus it does not need continuous feedback. The receiver needs to provide feedback only when the CSI variation, *i.e.*, the difference between the current and previously measured CSI, becomes significant. For this purpose, a threshold can be used in the reporting stage of the sensing procedure, which is described below in detail.

A diagram of the TSMR procedure proposed in this paper appears in Fig. 3, which is mainly composed of measurement and reporting stages. In the measurement stage, a transmitter sends a packet consisting of the data and pilot sequences, *i.e.*, Golay sequences, while a receiver utilizes the pilot sequences to estimate the channel for data detection. In the reporting stage, the receiver can further feedback the estimated CIR to the transmitter for sensing processing if it receives a feedback request from the transmitter. This feedback request from the transmitter may include the threshold for the receiver. After receiving the feedback request, the receiver subsequently checks for the CSI variation criterion, and depending upon the result, the receiver uses one-bit feedback to indicate whether they will perform further feedback or not. For example, if a significant change in the channel is detected, *i.e.*, the CSI variation is higher than the threshold, the receiver may send bit 1 and after receiving bit 1, the transmitter asks the receiver to feedback the estimated CIR measurement in the assigned resource unit¹ as shown in Fig. 3(a). On the contrary, the receiver transmits bit 0 if the criterion is not satisfied, and in this case, the transmitter can reconstruct the missing measurement using the previously received CIR measurements from the receiver, as depicted in Fig. 3(b). It is worth noting that due to this CSI variation criterion, some of the CIRs in the 2-D sensing data matrix may be missing, and in that case, we first reconstruct the missing CIRs and subsequently utilize them to build this matrix for Doppler processing in (8).

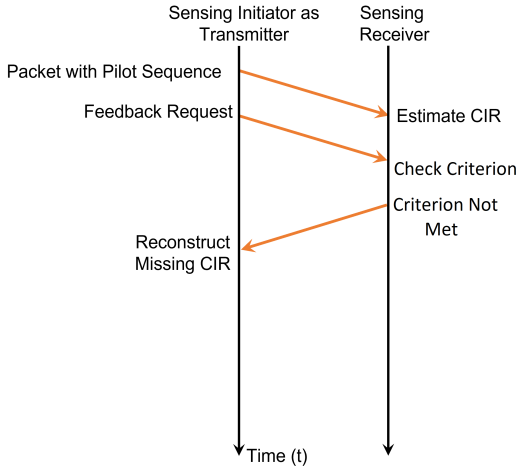
B. Calculation of CSI Variation

Depending on the sensing applications, different devices can employ different metrics to compute the channel variation.

¹The resource unit can comprise multiple sub-channels within the channel used by the transmitter.



(a) When CSI variation is greater or equal to the threshold



(b) When CSI variation is less than the threshold

Fig. 3: TSMR procedure where the packet including data and pilot sequence are used to estimate CIR for data detection and the estimated CIR is subsequently used for sensing upon receiving the feedback request from the initiator.

However, the computed CSI variation should normalize to a closed interval $[0, 1]$, where the value 0 represents that channel at two different time instants is completely identical and the value 1 represents that channel at two different time instants is entirely different. This normalization is important so that the initiator can decide the threshold within the range $[0, 1]$ for each device. In this work, we consider the following metrics to quantify the CSI variation between two consecutive CIRs $\hat{\mathbf{h}}_m$ and $\hat{\mathbf{h}}_{m-1}$ estimated using the m^{th} and $(m-1)^{\text{th}}$ transmitted packets.

1) *Euclidean Distance*: The normalized Euclidean distance $d(\hat{\mathbf{h}}_m, \hat{\mathbf{h}}_{m-1})$ between two CIRs $\hat{\mathbf{h}}_m$ and $\hat{\mathbf{h}}_{m-1}$ can be obtained as

$$d(\hat{\mathbf{h}}_m, \hat{\mathbf{h}}_{m-1}) = \sqrt{\frac{1}{2} \times \frac{\text{var}(\hat{\mathbf{h}}_m - \hat{\mathbf{h}}_{m-1})}{\text{var}(\hat{\mathbf{h}}_m) + \text{var}(\hat{\mathbf{h}}_{m-1})}}, \quad (9)$$

where the factor $1/2$ is used to bound $d(\hat{\mathbf{h}}_m, \hat{\mathbf{h}}_{m-1})$ between 0 and 1, and $\text{var}(\hat{\mathbf{h}} = [\hat{h}[l], \hat{h}[l+1], \dots, \hat{h}[l+L_G-1]])$ is

defined as

$$\text{var}(\hat{\mathbf{h}}) = \frac{1}{L_G} \sum_{i=0}^{L_G-1} \left(\hat{h}[i+l] - \frac{1}{L_G} \sum_{j=0}^{L_G-1} \hat{h}[j+l] \right)^2.$$

The CSI variation, denoted by ΔC , can be obtained as $\Delta C = d(\hat{\mathbf{h}}_m, \hat{\mathbf{h}}_{m-1})$. Note that if two CIRs are completely identical (i.e., $\hat{\mathbf{h}}_m = \hat{\mathbf{h}}_{m-1}$), the normalized Euclidean distance would be 0. On the other hand, the normalized Euclidean distance would be 1 for $\hat{\mathbf{h}}_m = -\hat{\mathbf{h}}_{m-1}$.

2) *Time-Reversal (TR) Resonating Strength*: The CSI variation can be obtained as $\Delta C = 1 - \text{TRRS}(\hat{\mathbf{h}}_m, \hat{\mathbf{h}}_{m-1})$, where the TR resonating strength $\text{TRRS}(\hat{\mathbf{h}}_m, \hat{\mathbf{h}}_{m-1})$ between two CIRs $\hat{\mathbf{h}}_m$ and $\hat{\mathbf{h}}_{m-1}$ can be derived as [14]

$$\text{TRRS}(\hat{\mathbf{h}}_m, \hat{\mathbf{h}}_{m-1}) = \frac{1}{\|\hat{\mathbf{h}}_m\| \|\hat{\mathbf{h}}_{m-1}\|} \times \max_{\tilde{i}=1,2,\dots,2L_G-1} |R_{\hat{\mathbf{h}}_m, \hat{\mathbf{h}}_{m-1}}[\tilde{i}]|, \quad (10)$$

where $R_{\hat{\mathbf{h}}_m, \hat{\mathbf{h}}_{m-1}}[\tilde{i}]$, $\tilde{i} = 1, 2, \dots, 2L_G - 1$ represents the cross-correlation between $\hat{\mathbf{h}}_m$ and $\hat{\mathbf{h}}_{m-1}$.

3) *Frequency-Reversal (FR) Resonating Strength*: Similar to TR resonating strength, the CSI variation can also be obtained by maximizing the subcarrier correlation in the frequency domain using the frequency-domain channel transfer functions. We refer to this metric as FR resonating strength. In this metric, the normalized CSI variation can be computed as $\Delta C = \frac{1}{2} \times \{1 - \text{FRRS}(\hat{\mathbf{H}}_m, \hat{\mathbf{H}}_{m-1})\}$, where $\text{FRRS}(\hat{\mathbf{H}}_m, \hat{\mathbf{H}}_{m-1})$ denotes the FR resonating strength between two frequency-domain channel transfer functions $\hat{\mathbf{H}}_m$ and $\hat{\mathbf{H}}_{m-1}$, which can be computed as

$$\text{FRRS}(\hat{\mathbf{H}}_m, \hat{\mathbf{H}}_{m-1}) = \frac{1}{\|\hat{\mathbf{H}}_m\| \|\hat{\mathbf{H}}_{m-1}\|} \times \max_{\tilde{i}=1,2,\dots,2N_{\text{ST}}-1} |R_{\hat{\mathbf{H}}_m, \hat{\mathbf{H}}_{m-1}}[\tilde{i}]|, \quad (11)$$

where N_{ST} is the number of subcarriers and $R_{\hat{\mathbf{H}}_m, \hat{\mathbf{H}}_{m-1}}[\tilde{i}]$, $\tilde{i} = 1, 2, \dots, 2N_{\text{ST}} - 1$ represents the correlation between $\hat{\mathbf{H}}_m$ and $\hat{\mathbf{H}}_{m-1}$. The frequency-domain channel transfer function $\hat{\mathbf{H}}_m$, defined as the Fourier transform of the impulse response $\hat{\mathbf{h}}_m$ at subband center frequency $f_{c,n}$, can be obtained as [15]

$$\hat{H}_m[f_{c,n}] = \sum_{l=0}^{L_G-1} \hat{h}_m[l] \exp(-j2\pi f_{c,n} l T_s), \quad (12)$$

where T_s is the sampling period and l is the tap index. Moreover, for a given wideband channel of bandwidth B and its center frequency f_c , the center frequency of the n^{th} subband can be obtained as, $f_{c,n} = f_c + n\Delta f$, where the subband spacing Δf considering the number of N_{ST} subbands is computed as, $\Delta f = \frac{B}{N_{\text{ST}}}$. Here $n = -\text{round}(\frac{N_{\text{ST}}}{2}) + 1, \dots, \text{floor}(\frac{N_{\text{ST}}}{2})$, where $\text{floor}(x)$ rounds the elements of x to the nearest integers towards $-\infty$ and $\text{round}(x)$ rounds towards the nearest decimal or integer.

To analyze the impact of these metrics on the CSI variation, we consider two different human movement cases, i.e., standing up and sitting down with four human subjects of different heights. These movements corresponding to two

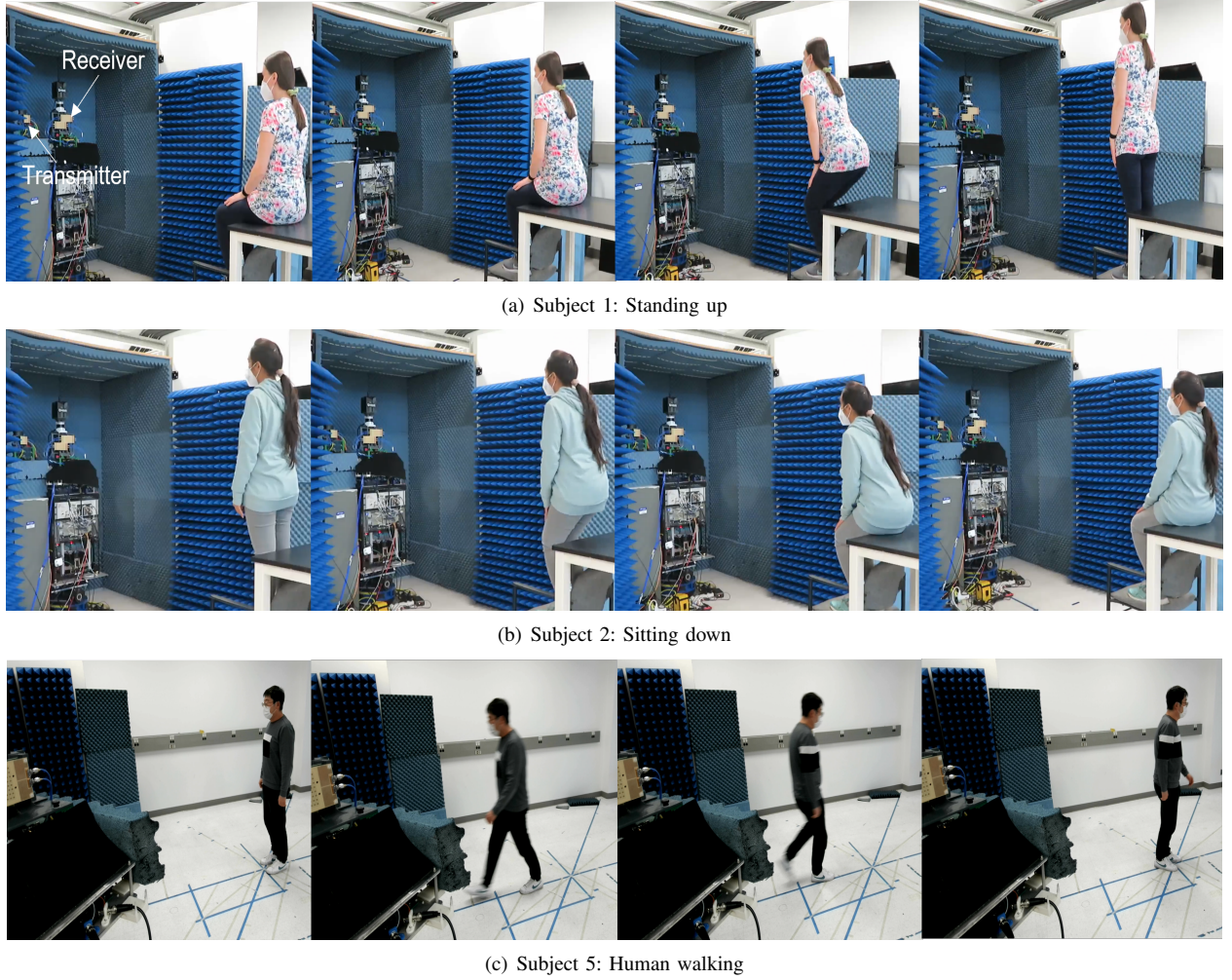


Fig. 4: Different human movements considered in the NIST measurement campaign.

human subjects, *i.e.*, subject 1 and subject 2, which are the part of the NIST measurement campaign², are shown in Figs. 4(a) and 4(b), respectively. Fig. 5 demonstrates the Doppler shift³ and corresponding CSI variations⁴ with the Euclidean distance, TRRS, and FRSS metrics for both the movements of all four subjects. For comparison purposes, we also include WiFi-based real-time human detection (WiSH) based metric proposed in [16], where the CSI variation is obtained as $\Delta C = 1 - \bar{c}_t \exp(0.1\bar{c}_f)$ and \bar{c}_t, \bar{c}_f denote the median time and frequency correlations, respectively. Here, median frequency correlation is calculated by using the N_{sel}

²The details of this channel measurement campaign are provided later on in Section V.

³To obtain the micro-Doppler spectrum in Fig. 5, the range-Doppler maps are summed over the range dimension, as described in Section II.B.4. Moreover, the Doppler shift is subsequently estimated by finding a point with the highest intensity in the micro-Doppler spectrum.

⁴Note that the time on the x -axis in both the micro-Doppler spectrum and the CSI variation plot depicts the total sensing duration across MN_{burst} sensing measurements. However, the time step in the CSI variation plot is smaller than in the micro-Doppler spectrum. The time step in the CSI variation plot equals the packet interval T_M , while the time step in the micro-Doppler spectrum is T since we have only N_{burst} range-Doppler maps or micro-Doppler spectrum obtained using the MN_{burst} sensing measurement feedback during the total sensing duration.

subcarriers selected randomly out of N_{ST} subcarriers, whereas \bar{c}_t is obtained by cross-correlating the complete CSI obtained at two different time-instants. As shown on the left side of each subfigure, our ISAC framework described in Section II-A can identify different Doppler signatures in both standing up and sitting down cases. It can be seen that standing up movement results in positive Doppler shift since the human body moves towards the receiver while standing up from sitting down position, whereas sitting down movement has negative Doppler shift since the subject moves away from the receiver. Interestingly, these positive and negative Doppler signatures are also consistent across all the subjects. On the other hand, one can also observe that each metric results in different normalized CSI variations, which can be seen on the right side of each subfigure. More specifically, the identical movements of subject 2 have significantly low CSI variation values compared to other subjects. However, the Euclidean distance metric, which quantifies the variation in the difference between two CIRs, can capture the standing up and sitting down motions of all human subjects with high CSI variation values. On the contrary, TRRS and FRSS metrics achieve almost identical CSI variation values most of the

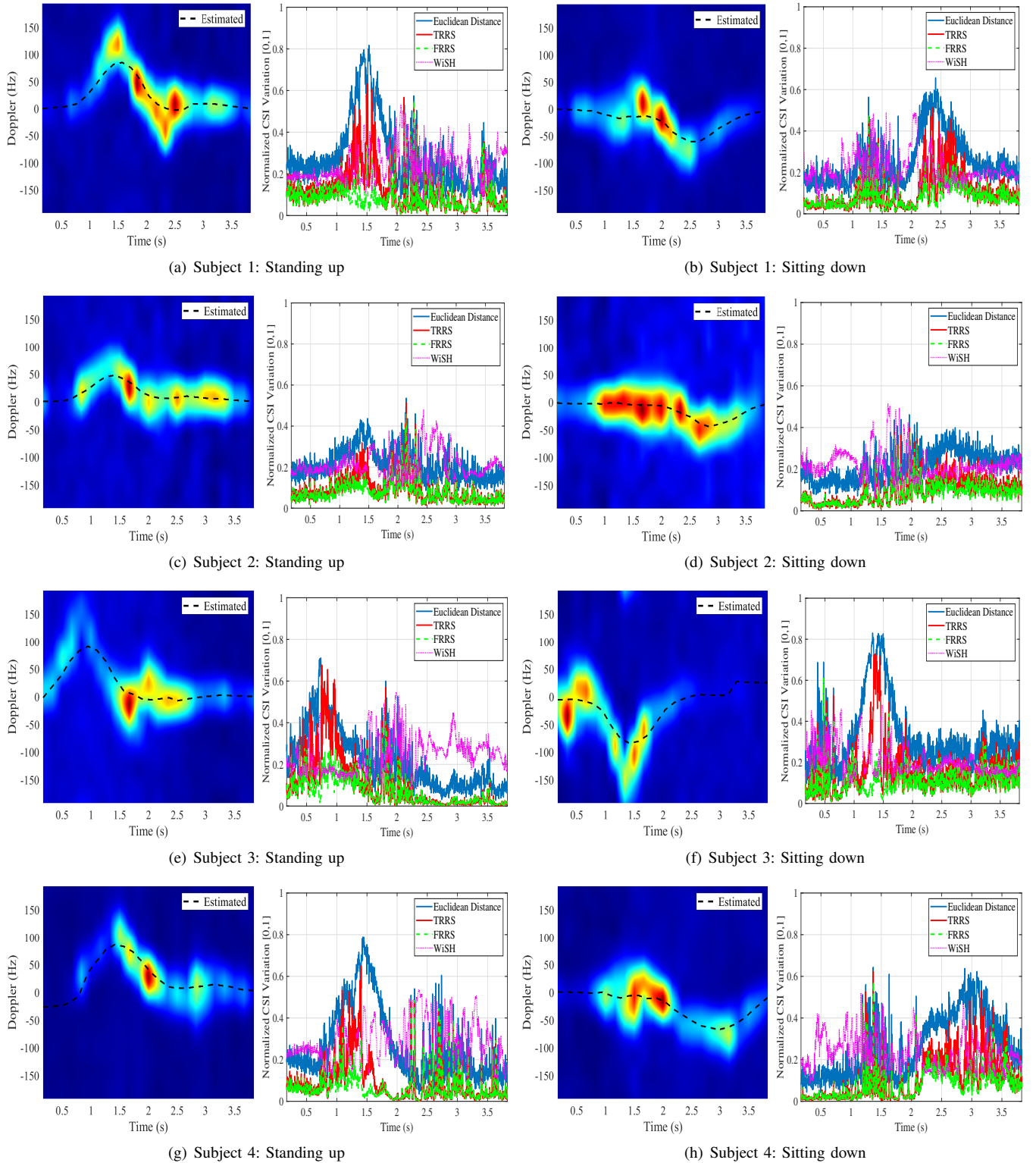


Fig. 5: Sensing performance and normalized CSI variation considering channel measurements obtained from measurement campaign, where the transmitter and receiver are placed such that normal of their arrays are forming 9° angle. Each subfigure shows the Doppler and corresponding normalized CSI variation. For Doppler processing, we consider packet repetition frequency (PRF) of 385 Hz, *i.e.*, $T_M=2.6$ ms, number of packets (M) in CPI as 64, Doppler FFT length N_ν as 512, Doppler FFT window and window length as Blackman-Harris and 16, respectively.

time and both metrics, especially FRRS, have less variation since the maximum amplitude of the entries of the cross-

correlation does not increase much in both human activities in the scenario. It is also interesting to observe that in contrast to

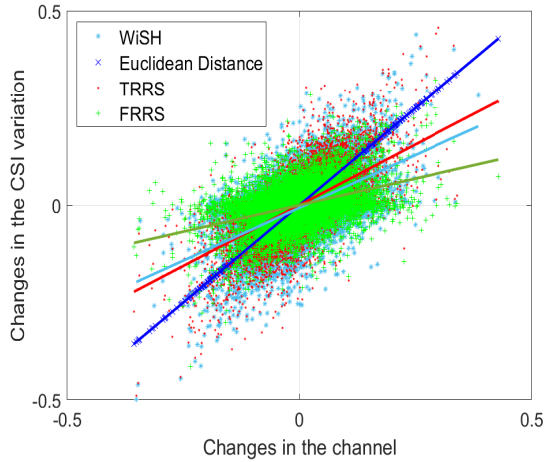


Fig. 6: Sensitivity of CSI variation metrics to channel changes considering real channel measurements for human walking scenarios. For WiSH, we consider $N_{\text{sel}} = 64$.

the WiSH metric, the Euclidean distance metric can capture the motions with high CSI variation values, especially when the human subject moves. In Fig. 6, we also analyze the sensitivity of CSI variation metrics to channel changes under real channel measurements for human walking scenarios with different human subjects. One of the human walking cases is shown in Fig. 4(c). In this result, we evaluate the changes in the channel through the Euclidean distance for each CSI variation metric and subsequently obtain the changes in the CSI variation. For better understanding, we also added a linear fit to each of the data. The slope of the linear fit indicates that the changes in the CSI variation are higher for the Euclidean distance metric in comparison to TRRS, FRRS and WiSH metrics. It can be observed that out of these metrics, the Euclidean distance metric is more sensitive to any small variations in the scenario. Moreover, WiSH based metric is more sensitive than FRRS since it leverages the cross-correlation in both time and frequency domains.

Next, we present reconstruction schemes that can improve sensing performance by reconstructing multiple CIR measurements at the transmitter.

C. Reconstruction Scheme for Missing CIR Measurements

As described in Fig. 3, the initiator reconstructs the CIR measurements for the time instants when the CSI variation criterion is not satisfied. This reconstruction to build a sensing data matrix for Doppler processing as shown in Fig. 1, is important because missing observations can lead to inaccurate sensing results at the initiator. Let $\hat{\mathbf{h}}_{m-k}$ and $\hat{\mathbf{h}}_m$ denote the channel measurements or measurements in complex CIRs received from the receiver corresponding to the $(m-k)^{\text{th}}$ and m^{th} packets transmitted by the transmitter, respectively. In this work, we propose two reconstruction schemes which can be considered at the initiator to reconstruct the missing channel measurements, *i.e.*, $\hat{\mathbf{h}}_{m-k+1}, \hat{\mathbf{h}}_{m-k+2}, \dots, \hat{\mathbf{h}}_{m-1}$ in between $\hat{\mathbf{h}}_{m-k}$ and $\hat{\mathbf{h}}_m$.

1) *Previous Measurement (No Interpolation) based Reconstruction*: In previous measurement-based reconstruction, the

missing channel measurements $\tilde{\mathbf{h}}_{m-k+i}$, $i = 1, 2, \dots, k-1$ can be directly reconstructed once it receives bit 0 from the receiver as

$$\tilde{\mathbf{h}}_{m-k+i} = \hat{\mathbf{h}}_{m-k}, \quad (13)$$

where $\hat{\mathbf{h}}_{m-k}$ represents the previously received measurement at initiator. This is due to the fact that if the CSI variation criterion does not satisfy, we assume that the channel at time instant t does not change compared to the previous time instant $t-1$ since there is no movement detected in the scenario. In case the initiator does not receive measurements in any of the time instants, *e.g.*, between the time instant 1 to $m-k$, channel measurement $\tilde{\mathbf{h}}_{m-k+i}$ would be identical to $\hat{\mathbf{h}}_0$ since the channel measurement at the start of the sensing procedure is always reported.

2) *Linear Interpolation based Reconstruction*: This scheme is based on linear interpolation of the values in each respective dimension, *i.e.*, real and imaginary. More specifically, each complex entry of missing CIRs is linearly interpolated using the complex entries of received CIRs at time $m-k$ and m as

$$\tilde{\mathbf{h}}_{m-k+i} = \hat{\mathbf{h}}_{m-k} + \frac{i}{k}(\hat{\mathbf{h}}_m + \hat{\mathbf{h}}_{m-k}). \quad (14)$$

In contrast to the previous reconstruction scheme, this scheme additionally involves measurement estimated using the m^{th} packet. For the case when the initiator does not receive any measurement corresponding to m^{th} packet, it uses the previous measurement as an interpolated one. Thus, for the scenario when the CSI variation criterion does not satisfy at any of the time instants *e.g.*, $m-k+1, \dots, m-1, m, m+1, \dots, M$, the linear interpolation reduces to the previous measurement-based reconstruction utilizing the estimated measurement $\hat{\mathbf{h}}_{m-k}$.

Next, we present an adaptive thresholding method, which can be employed at the transmitter to update the CSI variation threshold for the receiver in an adaptive fashion.

IV. ADAPTIVE THRESHOLD FOR CSI VARIATION CRITERION

Determining an accurate threshold to flag human movement is important. Note that if the transmitter sets this threshold as 0, the receiver feeds back the estimated CIR measurement at each time instant even if there is no movement in the environment. On the other hand, if it sets this threshold as 0.5, it does not mean that the transmitter will have feedback 50% of the time.

This can be seen in the Figs. 5(a) and 5(b) for subject 1, where the Euclidean distance metric assists the transmitter to have only 199 and 87 feedback messages out of 1500 under the standing up and sitting down cases, respectively. A similar observation can also be made in the case of other subjects when we set the threshold as 0.5. To capture the standing up and sitting down movements of these human subjects, the initiator should set the threshold lower than the normalized CSI variation values obtained using the CSI variation metric. For example, in the case of the Euclidean distance metric, the initiator should set the threshold lower than 0.2. For other TRRS and FRRS metrics, the CSI variation values are smaller than the Euclidean distance metric, as shown in Fig. 5. Thus, the threshold for TRRS and FRRS metrics should be lower

than the one used for the Euclidean distance to capture these movements. To avoid this dependency, we propose an adaptive threshold scheme that can be considered at the initiator to update the threshold adaptively by detecting the changes in the channel using the previously received measurements. With the adaptive-threshold method, instead of determining the minimum CSI variation for feedback, the objective is to adjust the CSI-variation threshold dynamically to optimize the sensing performance.

In this proposed method, the sensing duration is divided into multiple time intervals and in each time interval, the transmitter adaptively decides the threshold for the next time interval after detecting the movement through Doppler processing. It is worth noting that the duration of each interval *i.e.*, ΔT should be large enough such that the transmitter can perform Doppler FFT with the required packets per CPI. The parameter ΔT mainly depends on the Doppler processing capability of the transmitter, which can be considered as $\geq T$. For the case when $\Delta T = T$, it implies that the transmitter adaptively decides the threshold after each burst transmission of M packets. Note that if we consider a significantly higher value for ΔT and the sensing duration is not large enough, there is a possibility that the proposed method cannot follow the trend of CSI variation over time and does not result in a significant improvement over a fixed threshold scheme. Thus, to follow the trend of CSI variation over time, ΔT can be set as the minimum required value, *i.e.*, T . This adaptive threshold method for channel variation criterion is described in Algorithm 1 where the entire sensing duration for obtaining MN_{burst} sensing measurements is divided into multiple time intervals of duration ΔT . In this method, the initiator first initializes the threshold as γ , and based on this initial threshold setting, the receiver transmits the estimated CIR measurements if it satisfies the CSI variation criterion, *i.e.*, CSI variation is higher than the threshold γ . On the other hand, based on these CIR measurements feedback from the receiver, the initiator first reconstructs the missing CIR measurements if any, and subsequently performs Doppler processing, as presented in Section II-B3. Finally, based on the movement detection through detecting the peak, the initiator increases or decreases the threshold γ with a step size⁵ of $\Delta\gamma$ for the next duration of ΔT . More specifically, the initiator increases the threshold to reduce the number of feedback messages if there is no movement detected in the scenario. It is also important to note that when no movement of the target is detected for a long time, the initiator progressively increases the threshold to γ_{max} , and this high threshold value would significantly reduce the number of feedback messages. Furthermore, the parameter $N_F\%$ in Algorithm 1 denotes the number of feedback messages expected at the initiator in the duration of ΔT if any human movement is detected. For the case when the initiator detects the movement and the number of received feedback is not within the expected limit, *i.e.*, the number of received feedback is less than the expected number

⁵The value of $\Delta\gamma$ plays an important role because for low value $\Delta\gamma$, the proposed adaptive threshold scheme reduces to a fixed threshold scheme. On the other hand, for high value of $\Delta\gamma$, proposed scheme may reduce the number of feedback messages by approximately 50%.

Algorithm 1: Adaptive Threshold For Channel Variation criterion

```

Input: Initialize Threshold  $\gamma$ ,
          Threshold Step Size  $\Delta\gamma$ ,
          Maximum Threshold Limit  $\gamma_{\text{max}}$  if Human
          Movement is not Detected,
          Time Duration  $\Delta T$ ,
          Expected Number of Feedback Messages  $N_F\%$ 
          if Human Movement is Detected

Output: Threshold  $\gamma$ 
for each time duration of  $\Delta T$  do
  Estimate the Doppler using the reconstructed
  measurements when CSI variation  $\Delta C < \gamma$ 
  if Peak is detected then
    Calculate the percent of feedback (Feedback in
    %) using the received number of feedback
    messages
    if Feedback  $> N_F\%$  then
      |  $\gamma \leftarrow \gamma + \Delta\gamma$  or  $\gamma \leftarrow \gamma$ ;
    else
      |  $\gamma \leftarrow \gamma - \Delta\gamma$ ;
      | if  $\gamma < 0$  then
      | |  $\gamma \leftarrow 0$ 
      end
    end
  else
    |  $\gamma \leftarrow \gamma + \Delta\gamma$ 
    | if  $\gamma > \gamma_{\text{max}}$  then
    | |  $\gamma \leftarrow \gamma_{\text{max}}$ 
    end
  end
end
  
```

of feedback messages defined by $N_F\%$, the initiator decreases the threshold for the next duration of ΔT . This decrement in threshold value can allow the transmitter to receive more feedback in the next duration. In contrast, if it detects the movement and the number of received feedback is within the expected limit, the initiator can either increase the threshold or keeps the same threshold value. Note that the expected limit for $N_F\%$ can be set as 50 – 100%, where $N_F = 50\%$ denotes that the initiator expects at least 50% feedback if any movement is detected. For $N_F \leq 50\%$, the number of feedback messages keeps reducing which in turn affects the overall sensing performance at the transmitter. On the other hand, if the initiator expects $N_F = 100\%$ CIR measurements when there is a motion detected in the scenario, the algorithm progressively reduces the adaptive threshold to 0.

Fig. 7 demonstrates the impact of adaptive threshold over time considering sitting down and standing up movements of human subjects 1, 2, and 3, as described in Fig. 5. Particularly, in Figs. 7(a) and 7(b), we show the variation of adaptive threshold with respect to CSI variation metrics considering a fixed human subject, whereas in Figs. 7(c) and 7(d), we show the variation of adaptive threshold with respect to subjects considering a fixed CSI variation metric. It can be seen in Figs. 7(a)-7(d) that irrespective of the type of metric and subject, this

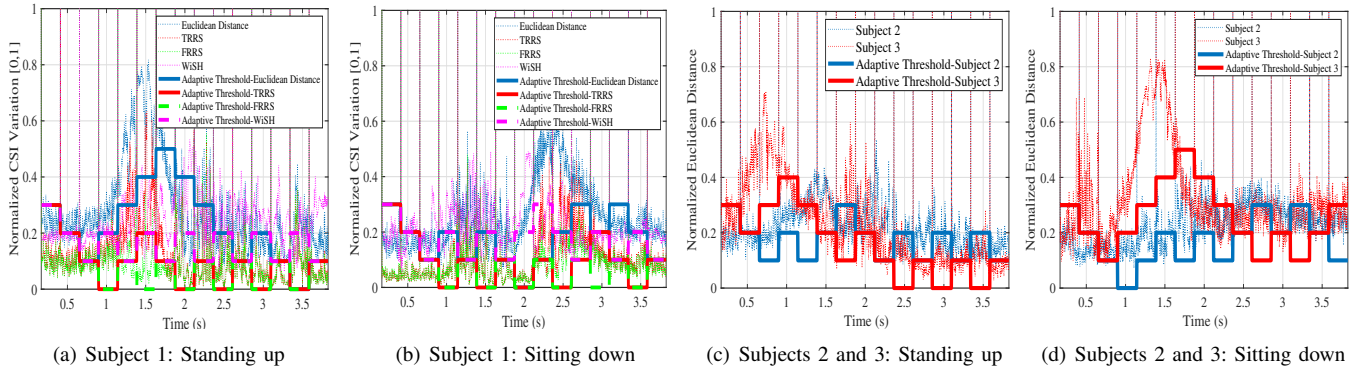


Fig. 7: Impact of adaptive thresholding over time for different CSI variation metrics and human subjects. For simulation, we divide the total time duration into 15-time intervals and in each time interval, the receiver obtains 100 CIR measurements. The other parameters in Algorithm 1 are set as, initial threshold $\gamma = 0.3$, step size $\Delta\gamma = 0.1$, maximum threshold limit $\gamma_{\max} = 1$, and we consider an increment of $\Delta\gamma$ if the number of received feedback is higher than $N_F = 95\%$.

method can optimize the sensing performance by dynamically choosing the threshold less than the CSI variation values for most of the times when there is a movement in the scenario. Interestingly, one can also observe that the adaptive threshold indirectly follows the trend of CSI variation over time, which reduces the number of feedback messages and also allows the transmitter to reconstruct the missing CIR measurements with better accuracy by using the nearby received measurements.

V. PERFORMANCE EVALUATION OF TSMR PROCEDURE

We consider a single access point (AP) initiator that is communicating via the SC waveform with a single responder [17]. These devices also participate in a sensing session considering the TSMR procedure, as described in Section III-A. In this case, the initiator transmits M data packets in a burst over a period of time T , and based on the channel variation metric criterion, a total of $K(\leq M)$ estimated CIR measurements are required to feedback from the responder. For the case when CSI variation criterion is not satisfied, the initiator reconstructs the missing $M - K$ CIR measurements using the schemes described in Section III-C. Based on these reconstructed measurements, the initiator can build the two-dimensional sensing data matrix, *i.e.*, the delay and the evolution over time to get the desired results, *e.g.*, compute the range and velocity or Doppler shift for motion detection after removing the clutter using a DC blocker, as described in Section II-A. In this work, we implement a DC blocker with a small recursive filter as described by a differential equation below.

$$\mathbf{op}_m = \mathbf{in}_m - \mathbf{in}_{m-1} + \alpha \mathbf{op}_{m-1},$$

where \mathbf{in}_m and \mathbf{op}_m are the current input and output samples, whereas \mathbf{in}_{m-1} and \mathbf{op}_{m-1} are the previous input and output samples, respectively. In the above equation, the parameter α determines the corner frequency and can be set in between 0.8 and 1. Note that as α approaches 1, the filter notch at DC gets narrower. In our evaluation, we consider α as 0.85.

In this paper, we consider an indoor room sensing use case with a focus on the range and velocity estimation of a moving

target. Mainly, we analyzed the impact of the TSMR procedure on the sensing accuracy, *i.e.*, mean-squared error (MSE) of range and velocity of the target. The MSE values for range and velocity estimates are calculated as follows

$$\text{MSE}_r(\text{dB}) = 10 \log_{10} \left(\frac{1}{N_{\text{burst}}} \|\mathbf{r}_{\text{gt}} - \hat{\mathbf{r}}\|^2 \right), \quad (15)$$

$$\text{MSE}_v(\text{dB}) = 10 \log_{10} \left(\frac{1}{N_{\text{burst}}} \|\mathbf{v}_{\text{gt}} - \hat{\mathbf{v}}\|^2 \right), \quad (16)$$

where the parameters \mathbf{r}_{gt} and \mathbf{v}_{gt} are the reference for the range and velocity of the target, respectively, whereas $\hat{\mathbf{r}}$ and $\hat{\mathbf{v}}$ denote the range and velocity estimates of the target that are obtained after processing the N_{burst} range-Doppler maps. Note that the reference for the range and velocity of the human target is obtained without missing any CIR measurements. To evaluate the performance of the TSMR procedure and also, to generate insights into the system performance, the extensive simulations are carried out using our open source NIST ISAC-PLM [18], [19] with the sensing-related parameters as mentioned in Table I. Moreover, we first utilize the NIST raytracing-based channel realization software [20] in Section V-A to generate the channel in the presence of a single human target, and later in Section V-B we use real channel measurements. Note that in both raytracing and real channel measurement cases, we convert the rays into the system level CIR⁶ (c.f. (3)) by utilizing the properties of each ray. Thus, our framework can be easily extended to other channel models or measurements if we can characterize each MPC in terms of complex amplitude, delay, and Doppler shift. Further note that in our evaluation, we consider burst transmissions, each burst consists of $M = 64$ packets with repetition frequency 385 Hz, to detect the maximum target velocity of ~ 1 m/s in all the indoor scenarios including the ones considered in real channel measurements. The repetition frequency of packets (PRF) determines the maximum velocity of the target that can be detected unambiguously. However, the max PRF is set by hardware limitations.

⁶The CIR generated is re-sampled at the system rate of 1.76 GHz.

TABLE I: Doppler Processing Parameters

System Parameter	Setting
Packet Repetition Frequency (PRF)	385 Hz
Packets in CPI (M)	64
Doppler FFT Length (N_ν)	512
Doppler FFT Window	Blackman-Harris
Window Length	16
Window Overlap	0

Fig. 8: Living room environment with the rays raytraced from the environment shown in black and from the target shown in blue.

A. Simulated Channel Measurement

To describe the environment and the interaction between the signals and the target(s), we adopt a raytracing-based channel model [21], which represents the human target using the Boulic model with $N_t = 17$ scattering centers [22]. This channel model performs 3D raytracing on environmental objects described by a 3D CAD model of the environment and a human target [23], [24] and provides the magnitude, phase, and time of arrival of individual propagation rays between multiple points in space. Each of the scattering centers is precisely raytraced, which can be seen in Fig. 8, to provide consistency in both spatial and time domains. Spatial and temporal consistency is a fundamental feature of a channel model to enable the study of sensing applications, for instance, to obtain realistic micro-Doppler description, which is the most common signal processing technique for extrapolating dynamic information such as the range and velocity of a moving target.

We consider a square living room environment⁷ of size $7\text{ m} \times 7\text{ m}$ with a ceiling height of 3 m, where a static AP initiator is communicating with a static responder or receiver over 60 GHz frequency band. The initiator is placed just below the ceiling on the left wall, whereas the receiver is attached to the right wall, as shown in Fig. 8 with red and blue spheres, respectively. This node arrangement is useful when the receiver is attached to the TV for receiving uncompressed high-definition video from an AP or set-top box. Under this setting, we generate 1000 different cases with the presence of a single human target. Each of the cases has a different channel variation since the target is randomly placed and has a different trajectory and velocity.

The sensing performance of the TSMR procedure considering the Euclidean distance, TRRS, and FRRS with the previous measurement based-reconstruction scheme under the raytracing-based channel model is demonstrated in Fig. 9, where the sensing accuracy is evaluated by considering the transmissions of $N_{\text{burst}} = 8$ bursts, each with $M = 64$ packets, over a sensing duration of 1.33 s for $S = 1000$ random human walking cases in the scenario. Particularly, in Fig. 9(a), we show the accuracy of the range and velocity estimates in terms

⁷The environment does not include the furniture and other objects to speed up the raytracing process. However, it is worth noting that these objects do not affect the sensing performance since we filter out the echoes from the static environment using clutter removal, as shown in Fig. 1.

of MSE, whereas Fig. 9(b) shows the number of feedback messages required for varying a threshold. Note that the MSE and the number of feedback messages required are calculated by averaging over S cases and the number of packets M transmitted in each case. It can be seen in Fig. 9(a) that the TRRS and FRRS metrics under human walking scenarios in raytracing-based channel have identical performance, whereas the Euclidean distance outperforms the TRRS and FRRS. This improvement arises because the Euclidean distance metric achieves high CSI variation values, which increase the number of feedback messages required for a given threshold as demonstrated in Fig. 9(b). One can also observe in Fig. 9(a) that after a certain threshold value, all the metrics experience a floor since the receiver forwards only one CIR measurement at the beginning. Fig. 9(c) also compares the MSE and number of feedback messages required of an adaptive threshold scheme with a fixed threshold for varying the threshold. Here, the threshold value on the x -axis represents the initial value used for the adaptive threshold, and the other parameters $\Delta\gamma$ and $N_F\%$ in Algorithm 1 are set as 0.1 and 90%, respectively. Moreover, we consider the Euclidean distance metric and previous measurement-based reconstruction scheme at the receiver and transmitter, respectively. It can be observed in Fig. 9(c) that the adaptive threshold with $\Delta T = 0.33\text{ s}$ improves performance by reducing the MSE values for range and velocity estimates while utilizing a comparable number of feedback messages. One can notice that for threshold = 0.1, a slight increment in the number of feedback messages for the adaptive threshold can improve the velocity and range estimates with MSEs of -3.1 dB and -1.4 dB , respectively, in comparison to -2.1 dB and 2 dB for fixed threshold. However, this improvement is not significant since the adaption could not keep up with the channel variation. It is because of the fact that $\Delta T = 0.33\text{ s}$ with a total sensing duration of 1.33 s allows the initiator to adapt the threshold four times. However, the major improvement of adaptive threshold method over a fixed threshold can be clearly seen when we reduce ΔT from 0.33 s to 0.16 s. This reduction allows the initiator to track the channel variation in a better way by adopting the threshold eight times.

B. Real Channel Measurement

In addition to analyzing the system through the raytracing-based channel model, it is also analyzed with measurements collected with our 28 GHz channel sounder [25], [26]. The antenna beamwidth at both the transmitter and receiver is 90° in azimuth and 50° in elevation; given the limited beamwidth, the antennas were pointed towards the targets of interest. The channel sounder has an instantaneous bandwidth of 2.16 GHz, equivalent to delay resolution of 0.5 ns (15 cm range). Per delay bin, the complex amplitude of the receiver power was recorded while maintaining phase synchronization between both ends via an optical cable. In this measurement campaign, the PRI of the probing signal was 2.6 ms, allowing a maximum unaliased Doppler velocity of 1 m/s. Note that these measurements are particularly useful to validate the results obtained from the raytracing-based channel model and also, to develop

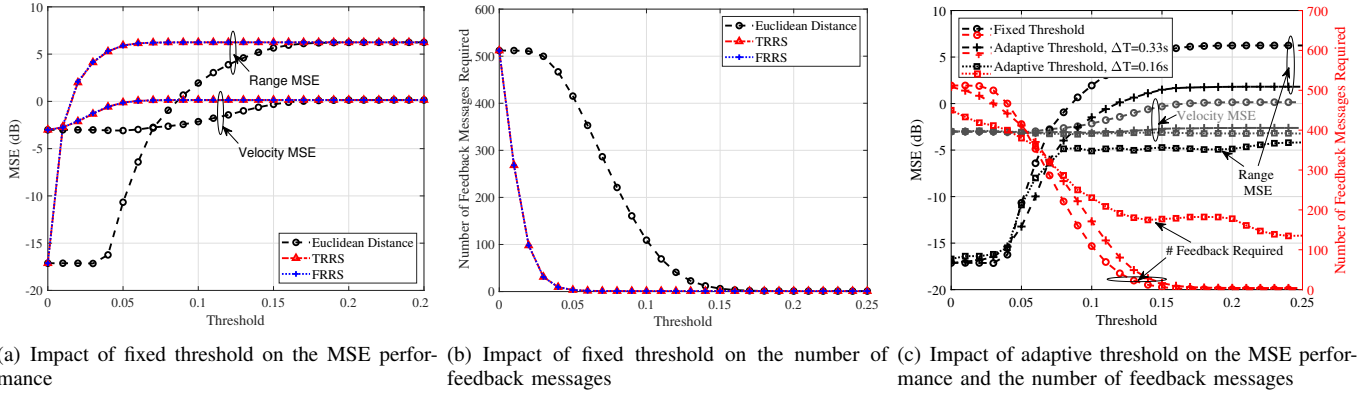


Fig. 9: Evaluation of TSMR procedure, where the performance is evaluated by averaging over 1000 different cases using the raytracing-based channel model and each case has random placement, trajectory, and velocity of the target. In Fig. 9(c), the curves and axes are color-coded.

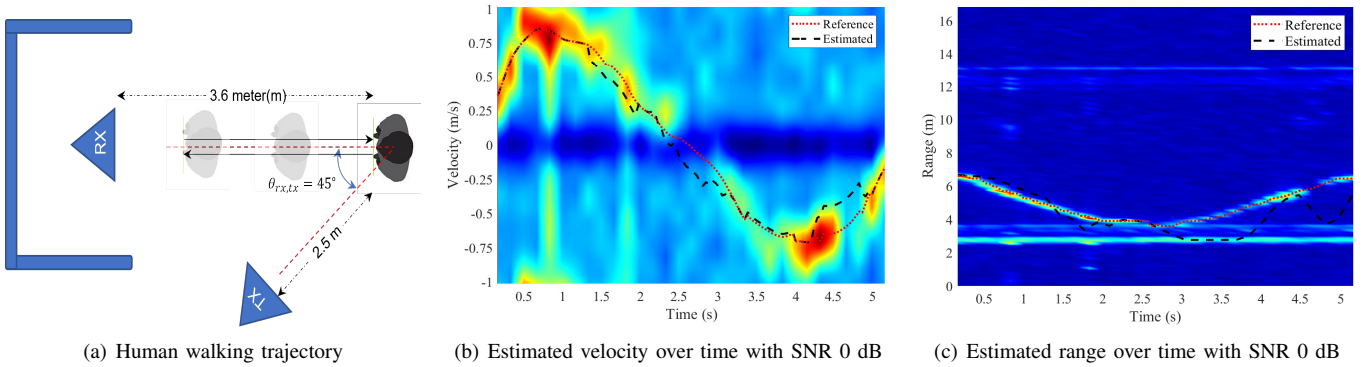


Fig. 10: Sensing performance evaluation, considering channel measurements obtained from measurement campaign. Here, to show the upper bound on the end-to-end system performance, we do not employ the TSMR procedure and consider that the receiver feeds back the measurements all the time to build a sensing data matrix for range and velocity estimation.

several interesting insights into the system performance in a real environment, as described below.

The measurement campaign was conducted in a room of size $14.1\text{ m} \times 7.1\text{ m} \times 3.3\text{ m}$, where the transmitter and the receiver are considered at the height of 1.55 m and 1.53 m, respectively. Based on this setup, the NIST is conducting an extensive channel measurement campaign to enable and analyze the sensing performance under various use cases or applications. One of the human walking scenarios, which is considered for evaluation unless otherwise stated, is described in detail below.

This scenario considers the placement of the transmitter and receiver such that the normal of their arrays intersect at a 45° angle. This can be seen in Fig. 10(a). Similar to the living room scenario considered in the raytracing-based channel model, the line-of-sight link in this setup is also available. Moreover, we considered that the human target walks directly towards the receiver and then turns 180° to walk away from the receiver in a total duration of 5.2 s, as shown through the black arrows in Fig 10(a). Fig. 10(b) depicts the micro-Doppler plot, which shows the variation of detected velocity of human target over time, whereas Fig. 10(c) shows the variation of the detected range of human target over time with operating signal-to-noise

ratio (SNR) of 0 dB. In Figs. 10(b) and 10(c), we do not employ the TSMR procedure and in that case, the receiver is available to feedback the estimated channel measurements all the time. Thus, the sensing performance at the transmitter is always limited by channel estimation errors. Moreover, for comparison purposes, the reference for velocity and range is obtained by considering all the 2000 channel realizations recorded during the 5.2 s and performed Doppler processing with the parameters mentioned in Table I. These references are consistent with the actual movement as described in Fig. 10(a). Interestingly, it can be observed in Figs. 10(b) and 10(c), that the Doppler processing can identify the movement of the target using the conventional IEEE 802.11ay-based pilot sequences [18]. Moreover, we can estimate the velocity and range most of the time even operating in the low SNR regime.

1) *Evaluation of variation metrics:* In Fig. 11(a), we show the variation of normalized CSI over time considering the metrics described in Section III-B for one of the human walking cases considered in our measurement campaign. For comparison purposes, we also include the WiSH-based metric proposed in [16], where N_{sel} is considered as 64. First, it can be seen that similar to standing up and sitting down motions in real channel measurements and human walking

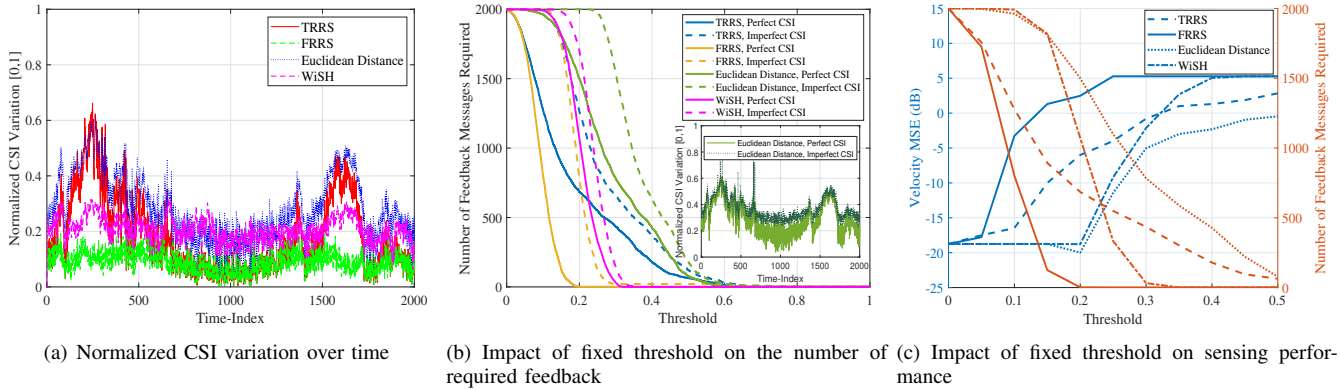


Fig. 11: Evaluation of TSMR procedure, considering real channel measurements for the human walking scenarios under different CSI variation metrics. In Fig. 11(b), the perfect CSI is obtained assuming an ideal transmission without noise. The imperfect CSI case is obtained by transmitting at SNR = 0 dB, such that the channel estimation is prone to errors due to noise.

in a raytracing-based channel model, the Euclidean distance metric also achieves a higher normalized CSI variation value for the human walking scenario considered in real channel measurement. Second, one can observe that the FRRS metric is less sensitive to the variations that occurred in the channel due to the motion of the human target. On the other hand, TRRS and FRRS experience identical normalized CSI variation values more than 50% of the time and for both metrics, the threshold value needs to be significantly low to capture complete human motion throughout the time to achieve better accuracy. Furthermore, one can also observe that the normalized CSI variation values for the WiSH-based metric are higher in comparison with FRRS since FRRS only employs cross-correlation in the frequency domain, whereas WiSH leverages cross-correlation in both frequency and time domains. Fig. 11(b) further demonstrates the impact of the threshold on the number of feedback messages required from the responder to the AP initiator. For each metric, the number of CIR measurements that need to be sent back reduces as the threshold increases. Moreover, since the Euclidean distance metric is more sensitive to any small variations in the scenario, it will trigger feedback more often. On the other hand, one can also observe that for a given threshold, the WiSH metric results in a higher number of feedback in comparison with FRRS. Moreover, for a low value of the threshold, *i.e.*, $\gamma < 0.2$, the WiSH metric results in a higher number of feedback in comparison with TRRS, whereas for $\gamma > 0.2$, the TRRS metric results in a higher number of feedback. Interestingly, the channel variation value increases as the SNR decreases, which can be seen in the sub-figure in Fig. 11(b). This is due to the fact that in the low SNR regime, the channel cannot be estimated accurately and due to the high estimation error, the channel changes drastically which in turn results in higher channel variation values. Therefore, if we consider a low value of the threshold *e.g.*, 0.2 in the low SNR regime, the responder transmits CIR measurements in each time instant and in this case, the sensing performance is always limited by the channel estimation errors. Moreover, one can also observe in Fig. 11(c) that each metric has a different number of required feedback for a fixed value of the threshold, which in

turn results in different sensing performances. For example, if the AP initiator sets the fixed threshold at 0.15, FRRS, TRRS, WiSH, and Euclidean distance metrics estimate the velocity with MSEs of 1.3 dB, -10.03 dB, -18.75 dB, and -18.7 dB with the reduction in the number of required feedback by 93.75%, 53.35%, 9.1%, and 9.4%, respectively.

2) *Evaluation of adaptive threshold:* In contrast to Fig. 9(c) where we considered the raytracing-based channel model, Fig. 12 analyzes the sensing performance of the adaptive threshold method and compares it against the fixed threshold method under real human walking channel measurement. Similar to Fig. 9(c), the threshold value on the x -axis in Figs. 12(b) and 12(c) represents the initial value used for the adaptive threshold, and the step size $\Delta\gamma$ in Algorithm 1 is set as 0.1. Moreover, the receiver employs the Euclidean distance-based CSI variation metric, whereas the transmitter uses the previous measurement-based reconstruction with the number of expected feedback $N_F = 90\%$ if human motion is detected. As described in Section IV, the proposed adaptive threshold method optimizes the sensing performance by dynamically setting the threshold less than the CSI variation values most of the time when there is a movement in the scenario. Thus, for the low value of the initial threshold *e.g.*, $\gamma = 0$, the number of feedback messages required in the adaptive threshold is lower compared to the fixed threshold. However, the MSE performance in terms of velocity and range estimates is comparable, which can also be seen in Figs. 12(b) and 12(c). On the other hand, as the threshold value increases, the number of feedback messages required progressively reduces in the case of a fixed threshold, which in turn deteriorates the sensing performance. However, for the same initial threshold value, the sensing performance can be enhanced in the case of an adaptive threshold since it can dynamically follow the trend of CSI variation over time and transmits more feedback messages when there is a movement detected in the scenario. Further, as seen in Fig. 12(a), the adaptive algorithm with initial threshold $\gamma = 0.25$ progressively decreases the threshold in the second and third duration since the initiator detects the peak and the number of received feedback messages is less than the expected number of feedback messages. However, the initiator

increases the threshold in the fourth duration since, in the third duration, the number of feedback messages received is higher than expected. It is worth noting that this adaptive threshold with initial threshold $\gamma = 0.25$ reduces the number of feedback messages by approximately 50%. However, it can estimate the velocity and range with MSEs -11.2 dB and -5.4 dB, as shown in Figs. 12(b) and 12(c), respectively.

3) *Evaluation of step size*: Fig. 13 further evaluates the sensing performance for varying the step size under the real channel measurement for the human walking scenario. Particularly, in Fig. 13(a), we obtain the number of feedback messages required by varying the step size and initial threshold in the adaptive threshold method, where the number of feedback messages required is color-coded. Subsequently, in Fig. 13(b)-(c), we present their corresponding impact on the sensing performance where MSE values are color-coded. It can be clearly seen that except for small step sizes at a higher initial threshold, the proposed adaptive threshold method can track the channel variation most of the time and capture the range and velocity of the target with lower MSE values by utilizing more than 800 sensing measurements. For small step sizes at a higher value of the initial threshold, the number of feedback messages required is remarkably low since threshold adaption with low step size cannot keep up with the channel variation. However, as the step size increases with a high value of the initial threshold, the number of feedback messages increases, which in turn improves the sensing performance. Apart from this, for varying initial threshold with a fixed value of step size e.g., $\Delta\gamma = 0.1$, increasing and decreasing behavior of the number of feedback messages arise since based on the initial threshold, the initiator tries to adjust the threshold to receive at least $N_F\% = 90\%$ feedback and once it receives $N_F\% = 90\%$ feedback, it increases the threshold that in turns reduce the number of feedback messages. This increasing and decreasing behavior of the number of feedback messages for varying the initial threshold with a fixed step size can be clearly seen in Fig. 12(b).

Table II analyzes the impact of adaptive threshold on the sensing performance, considering different reconstruction schemes under perfect and imperfect channel estimates. Note that the first value in each column corresponds to channels estimated at a high SNR regime with negligible noise, denoted as perfect channel estimation as the performance degradation due to added noise can be ignored, whereas the second value corresponds to imperfect channel estimates with 0 dB SNR. First, it can be observed that under perfect and imperfect channel estimates, the Euclidean distance and TRRS metrics perform better with significantly low MSE values for both range and velocity estimations. Second, in contrast to a fixed threshold where operating in the low SNR regime results in a higher number of feedback messages required, the adaptive threshold with the Euclidean distance metric reduces the number of feedback required from 1781 to 1373. This is due to the fact that the adaptive threshold algorithm set, $N_F = 90\%$ which increases the threshold by step size if the initiator receives more than 90% of the measurements. However, this decrease in the number of feedback required under the Euclidean distance metric does not degrade the

performance. On the other hand, TRRS and FRRS result in a higher number of feedback messages required if we operate in the low SNR regime. Similar to the Euclidean distance, both the reconstruction schemes in TRRS perform well and performance further improves under a low SNR regime due to an increase in the number of feedback messages. However, this increase in the number of feedback in the low SNR regime does not significantly improve the performance in FRRS considering these reconstruction schemes.

For a fair comparison of these interpolation schemes, we also evaluate the sensing performance considering a fixed number of feedback messages under perfect channel estimates at high SNR. Here, we obtain the fixed number of feedback messages by considering different threshold values for each CSI variation metric. Interestingly, one can observe in Table III that with a fixed number of feedback messages, all the schemes result in significantly low MSE values, but linear interpolation works better than the other two schemes across all the CSI variation metrics. This observation can also be seen for the adaptive threshold in Table II. This improvement arises since the linear interpolation scheme uses previous and next received CSI measurements for interpolation.

Further, to demonstrate the impact of different topologies on the sensing performance employing the TSMR procedure, we considered additional channel measurements recorded for five different human walking cases. These five new cases are shown in Fig. 14, where the transmitter is located at a fixed location, whereas the receiver is situated in a different location, and a human subject is moving towards it. As mentioned earlier, if we employ the same CSI variation metric e.g., Euclidean distance in a given scenario with a different location of communicating nodes and target, CSI variation values would be different. This can also be seen in Figs. 15(a) and 15(b), where CSI variation values in 90° case are comparatively lower than the 9° case. Now, if we employ a fixed threshold e.g., $\gamma = 0.2$, the sensing performance using the TSMR procedure would be different in both cases. To avoid this dependency, the TSMR procedure with an adaptive thresholding scheme can be used, which can significantly improve the sensing performance by following the trend of CSI variation over time under any scenario or topology with the arbitrary placement of communication devices and human targets. To analyze this improvement, the performance of the TSMR procedure with fixed and adaptive thresholding methods under these five different topologies is presented in Table IV, where γ in fixed and adaptive threshold methods is set as 0.2. It can be observed that in comparison to the other four cases, the 90° case only has 190 feedback messages (c.f. Fig. 15(b)) and results in very poor sensing performance for a fixed threshold. However, if an adaptive thresholding scheme proposed in Section IV is employed, the sensing performance in all five cases is significantly improved, which validates that the TSMR procedure with an adaptive thresholding scheme can be used for any scenario with the arbitrary placement of communication devices and human target.

Finally, to evaluate the impact of sensing on communication performance, we analyze the sensing overhead (OH) in Table IV for both fixed and adaptive thresholding schemes in the

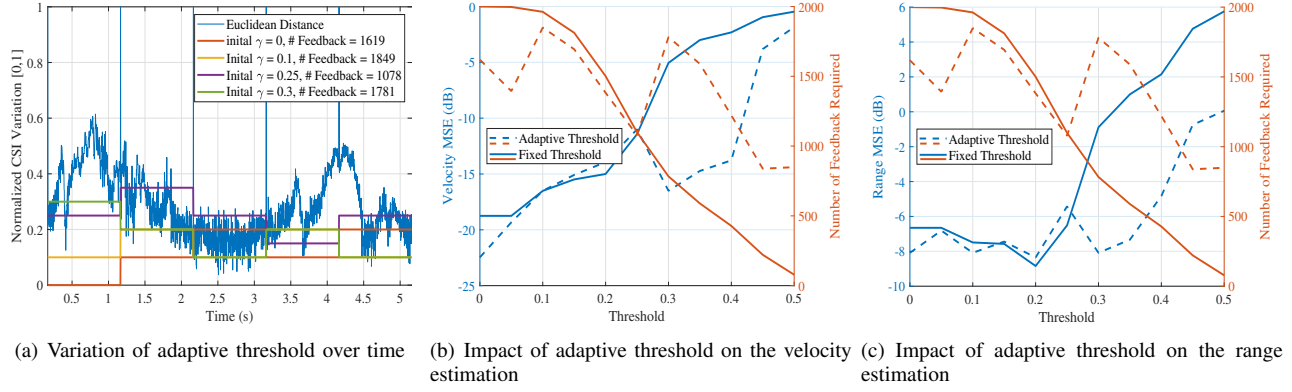


Fig. 12: Sensing performance evaluation, considering TSMR procedure with adaptive threshold scheme under real channel measurements

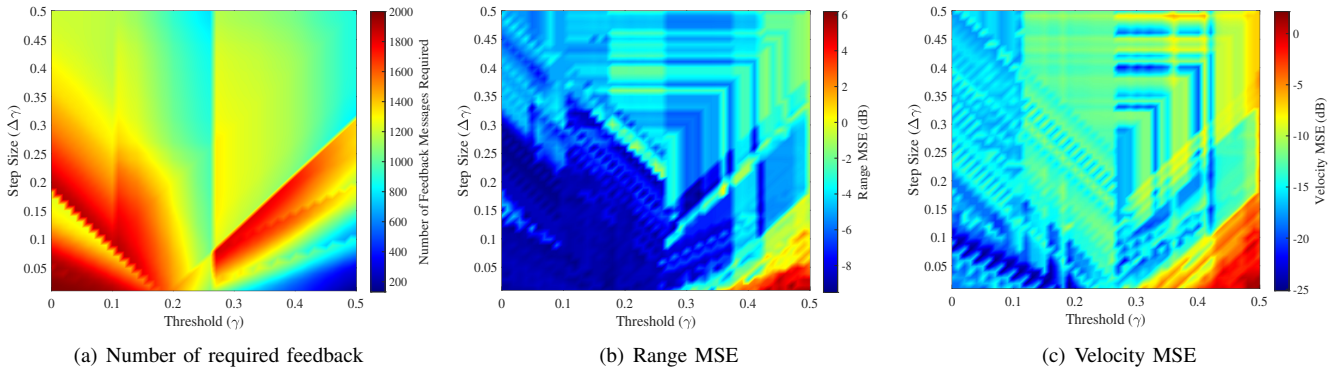


Fig. 13: Impact of step size on the MSE performance and the number of feedback messages considering adaptive threshold scheme in real channel measurements for human walking scenario.

TABLE II: Adaptive Threshold with fixed initial threshold = 0.3 where the first value in each column corresponds to perfect channel estimates at high SNR, whereas the second value corresponds to imperfect channel estimates with 0 dB SNR

Reconstruction Scheme	Euclidean Distance		TRRS		FRRS	
	# Feedback Required=1781, 1373		# Feedback Required=1068, 1694		# Feedback Required=570, 1210	
Previous Measurement	Range MSE	Velocity MSE	Range MSE	Velocity MSE	Range MSE	Velocity MSE
Linear Interpolation	-8.08, -7.80	-16.50, -16.26	-2.35, -8.32	-7.90, -11.51	3.23, -1.10	0.55, -0.19
	-8.99, -8.27	-16.99, -16.29	-2.59, -8.62	-10.93, -15.42	-0.20, -1.19	-0.40, -2.33

TABLE III: Impact of reconstruction schemes considering a fixed number of feedback messages = 1000 under perfect channel estimates at high SNR

Reconstruction Scheme	Euclidean Distance		TRRS		FRRS	
	Threshold = 0.2633		Threshold = 0.134		Threshold = 0.09	
	Range MSE	Velocity MSE	Range MSE	Velocity MSE	Range MSE	Velocity MSE
Previous Measurement	-6.90	-10.6	-7.16	-9.78	-4.40	-6.02
Linear Interpolation	-6.92	-10.93	-7.81	-9.95	-11.32	-6.15

TSMR procedure. Here, the sensing OH corresponding to the transmissions of N_{burst} bursts, each consists of M packets with the symbol rate $1/T_S = 1.76 \times 10^9$ symbol per second (sps), is calculated as

$$\text{OH}(\gamma) = \frac{1}{N_{\text{burst}}M} [\text{OH}_{\text{first}} + \text{OH}_{\text{second}}(\gamma)] \times 100 \%, \quad (17)$$

where the sensing OH is a function of the threshold γ used in the TSMR procedure. The first overhead term OH_{first} in the above expression, which does not depend on γ , is calculated for the second and third messages exchanged between the

transmitter and receiver after transmitting the data packet with pilot sequence (c.f. Fig. 3 in Section III-A) as

$$\text{OH}_{\text{first}} = MN_{\text{burst}}(L_{\text{msg},1} + L_{\text{msg},2})T_S \times \text{PRF}, \quad (18)$$

and $\text{OH}_{\text{second}}(\gamma)$ is calculated for the fourth and fifth messages, which are only exchanged for collecting the CSI measurements when the CSI variation criterion is satisfied at the receiver, as

$$\text{OH}_{\text{second}}(\gamma) = N_{\text{met}}(L_{\text{msg},3} + L_{\text{msg},4})T_S \times \text{PRF}, \quad (19)$$

where $N_{\text{met}}(\leq N_{\text{burst}}M)$ denotes the number of times the CSI variation criterion is met and $L_{\text{msg},i}$, $i \in \{1, 2, 3, 4\}$

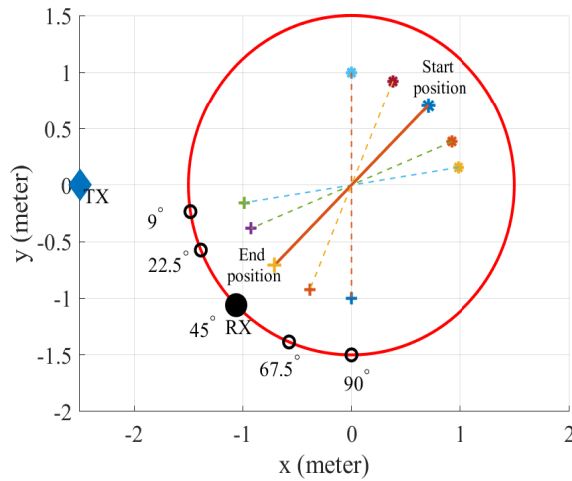


Fig. 14: Measurement setup for the human walking scenario with five different topologies, where the human subject walks towards the receiver in a straight line between the start and end positions. This scenario considers the placement of the transmitter and receiver such that the normal of their arrays intersect at an angle α , where α is considered as 9° , 22.5° , 45° , 67.5° and 90° .

is the length of the i th message, which consists of data and preamble fields of size 4096 and 560 bytes, respectively. For simplicity, we consider the same size for the data fields in each message. One can observe in Table IV that the OH introduced to enable sensing with the TSMR procedure is below 3% for both fixed and adaptive thresholding schemes. However, for the case when $N_{\text{met}} = N_{\text{burst}}M$, i.e., the CSI variation criterion is always met as shown in Fig. 3(a), the maximum resources occupied by the sensing messages are 3.25% of the symbol rate.

VI. CONCLUSION

In this paper, we considered the threshold-based sensing measurement and reporting procedure which is recently introduced by the IEEE 802.11bf task group to reduce the number of feedback messages required to report the channel measurements for sensing applications. We extended this procedure using the IEEE 802.11ay SC communication waveform, which enabled us to analyze threshold-based sensing performance with channel measurements estimated using the conventional IEEE 802.11ay pilot sequences. Furthermore, based on various CSI variation and reconstruction schemes, we developed several important insights into the system performance under synthetic and real channel measurements where the Euclidean distance-based CSI variation metric can best capture various human movements. Apart from this, the linear interpolation scheme results in a better performance. Furthermore, we demonstrated that in contrast to a fixed threshold, the proposed adaptive threshold at the initiator can further improve the sensing performance. Finally, our experimental results showed that the adaptive threshold can reduce the number of feedback messages by approximately 50%, while estimating the human

velocity and range with MSEs -11.2 dB and -5.4 dB, respectively, under real channel measurements.

Future studies can now focus on several research directions. For instance, researchers could investigate how the TSMR procedure performs in the presence of multiple human targets, which are often present in outdoor environments. Moreover, optimizing the step size for each duration of ΔT in the adaptive-threshold method may be beneficial to further improve the sensing performance at the transmitter. One effective way to achieve this is by leveraging the previously received CIR measurements at the transmitter. Lastly, the CSI variation criteria used in the TSMR procedure could be employed to promote collaborative sensing, allowing multiple devices to collaborate only when they observe a significant variation in the channel. These research directions hold immense promise in improving the effectiveness of the TSMR procedure and can have a significant impact on various sensing applications.

REFERENCES

- [1] F. Liu, Y. Cui, C. Masouros, J. Xu, T. X. Han, Y. C. Eldar, and S. Buzzi, "Integrated sensing and communications: Towards dual-functional wireless networks for 6G and beyond," *IEEE Journal on Selected Areas in Communications*, vol. 40, no. 6, pp. 1728–1767, 2022.
- [2] F. Liu, L. Zhou, C. Masouros, A. Li, W. Luo, and A. Petropulu, "Toward dual-functional radar-communication systems: Optimal waveform design," *IEEE Transactions on Signal Processing*, vol. 66, no. 16, pp. 4264–4279, 2018.
- [3] Y. Cui, F. Liu, X. Jing, and J. Mu, "Integrating sensing and communications for ubiquitous iot: Applications, trends, and challenges," *IEEE Network*, vol. 35, no. 5, pp. 158–167, 2021.
- [4] A. Kasher and et al., *WiFi-Sensing-Use-Cases*, IEEE Std. IEEE 802.11-21-1712-02, 2021.
- [5] J. Wang, N. Varshney, C. Gentile, S. Blandino, J. Chuang, and N. Golmie, "Integrated sensing and communication: Enabling techniques, applications, tools and data sets, standardization, and future directions," *IEEE Internet of Things Journal*, vol. 9, no. 23, pp. 23 416–23 440, 2022.
- [6] *Part 11: Wireless LAN Medium Access Control (MAC) and Physical Layer (PHY) Specifications—Amendment 2: Enhancements for Wireless LAN Sensing*, IEEE Std. IEEE P802.11bf/D1.1, 2022.
- [7] T. Ropitault, C. R. C. M. da Silva, S. Blandino, A. Sahoo, N. Golmie, K. Yoon, C. Aldana, and C. Hu, "IEEE 802.11bf WLAN sensing procedure: Enabling the widespread adoption of Wi-Fi sensing," *IEEE Communications Standards Magazine*, 2023.
- [8] R. Du and et al., *Truncated Power Delay Profile - follow up*, IEEE Std. IEEE 802.11-21-1288-04, 2021.
- [9] M. Hu and et al., *Threshold based sensing measurement*, IEEE Std. IEEE 802.11-21-0351-05, 2021.
- [10] R. Yang and et al., *Discussion on Threshold-based Sensing*, IEEE Std. IEEE 802.11-22-0328-02, 2022.
- [11] *Part 11: Wireless LAN (MAC) and (PHY) Specifications—Amendment 2: Enhanced Throughput for Operation in License-Exempt Bands Above 45 GHz*, IEEE Std. IEEE P802.11ay/D7.0, 2020.
- [12] F. Colone, K. Woodbridge, H. Guo, D. Mason, and C. J. Baker, "Ambiguity function analysis of wireless LAN transmissions for passive radar," *IEEE Transactions on Aerospace and Electronic Systems*, vol. 47, no. 1, pp. 240–264, 2011.
- [13] *Channel Models for IEEE 802.11ay*, IEEE P802.11 Group for Wireless Local Area Networks (LANs) Std. IEEE 802.11-15/1150r9, 2015.
- [14] Z.-H. Wu, Y. Han, Y. Chen, and K. R. Liu, "A time-reversal paradigm for indoor positioning system," *IEEE Transactions on Vehicular Technology*, vol. 64, no. 4, pp. 1331–1339, 2015.
- [15] N. Varshney, J. Zhang, J. Wang, C. Gentile, and N. Golmie, "Link-level abstraction of IEEE 802.11ay based on quasi-deterministic channel model from measurements," in *2020 IEEE Vehicular Technology Conference (VTC2020-Fall)*, 2020, pp. 1–5.
- [16] T. Hang, Y. Zheng, K. Qian, C. Wu, Z. Yang, X. Zhou, Y. Liu, and G. Chen, "Wish: Wifi-based real-time human detection," *Tsinghua Science and Technology*, vol. 24, no. 5, pp. 615–629, 2019.

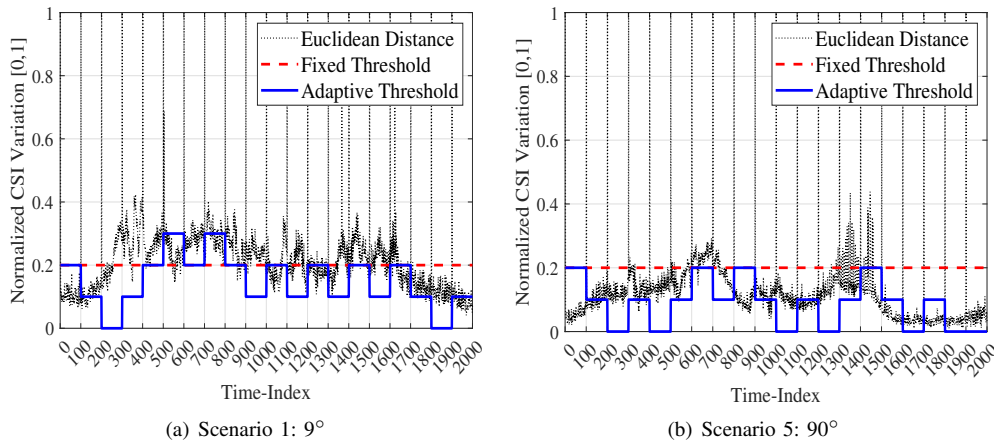


Fig. 15: Variation of adaptive threshold over time considering human walking scenario with two different topologies.

TABLE IV: Comparison of fixed and adaptive thresholding methods under various network topologies

Scenario	Fixed Threshold				Adaptive Threshold			
	# Feedback Required	Range MSE	Velocity MSE	OH	# Feedback Required	Range MSE	Velocity MSE	OH
9°	1081	-3.7	-15.15	2.51%	1421	-10.8	-23.6	2.78%
22.5°	1421	-4.5	-17.42	2.78%	1573	-15.4	-25	2.91%
45°	1328	-2.9	-13.9	2.71%	1125	-7.8	-22.5	2.54%
67.5°	1014	-2.6	-14.16	2.45%	1254	-9.4	-24.3	2.65%
90°	190	7.3	4.6	1.78%	1149	-6.9	-18.65	2.56%

- [17] S. Blandino, T. Ropitault, N. Varshney, J. Wang, J. Senic, J. Chuang, C. Gentile, and N. Golmie, *DMG/EDMG Link Level Simulation Platform*, IEEE Std. IEEE 802.11-22-0803-00, 2021.
- [18] S. Blandino, N. Varshney, J. Wang, and J. Zhang, “Integrated sensing and communication physical layer model (isac-plm),” <https://github.com/wigig-tools/isac-plm>, 2022.
- [19] S. Blandino, T. Ropitault, C. R. C. M. da Silva, A. Sahoo, and N. Golmie, “IEEE 802.11bf DMG sensing: Enabling high-resolution mmWave Wi-Fi sensing,” *IEEE Open Journal of Vehicular Technology*, vol. 4, pp. 342–355, 2023.
- [20] A. Bodi, S. Blandino, N. Varshney, J. Zhang, T. Ropitault, M. Lecci, P. Testolina, J. Wang, C. Lai, and C. Gentile, “A quasi-deterministic (Q-D) channel implementation in MATLAB software,” <https://github.com/wigig-tools/qd-realization>, 2021.
- [21] S. Blandino, T. Ropitault, A. Sahoo, and N. Golmie, “Tools, models and dataset for ieee 802.11 ay csi-based sensing,” in *2022 IEEE Wireless Communications and Networking Conference (WCNC)*. IEEE, 2022, pp. 662–667.
- [22] R. Boulic, N. Magnenat-Thalmann, and D. Thalmann, “A global human walking model with real-time kinematic personification,” *Vis. Comput.*, vol. 6, no. 6, p. 344–358, Nov. 1990. [Online]. Available: <https://doi.org/10.1007/BF01901021>
- [23] S. Blandino, T. Ropitault, N. Varshney, and N. Golmie, *A preliminary channel model using ray-tracing to detect human presence*, IEEE Std. IEEE 802.11-21-0747-01, 2021.
- [24] M. Zhang and et al., *Channel Models for WLAN Sensing Systems*, IEEE Std. IEEE 802.11-21/0782r5, 2022.
- [25] S. Y. Jun, J. Chuang, D. Caudill, C. Gentile, S. Blandino, and N. Golmie, *NIST mmWave Phased-Array Channel Sounder for Human Sensing*, IEEE Std. IEEE 802.11-21-1675-01, 2021.
- [26] D. Caudill, J. Chuang, S. Y. Jun, C. Gentile, and N. Golmie, “Real-time mmwave channel sounding through switched beamforming with 3-D dual-polarized phased-array antennas,” *IEEE Transactions on Microwave Theory and Techniques*, vol. 69, no. 11, pp. 5021–5032, 2021.